Word count: 5965

Deformation and Strength of Mantle Relevant Garnets: Implications for the Subduction of Basaltic-rich Crust

Cara E. Vennari[1,2*], Feng Lin[2], Martin Kunz[3], Masaki Akaogi[4], Lowell Miyagi[2], and Quentin Williams[5]

[1]Department of Geophysical Sciences, University of Chicago, Chicago, Illinois 60637, USA. [2]Geology and Geophysics, University of Utah, Salt Lake City, Utah 84112, USA. [3]Advanced Light Source, Lawrence Berkeley National Laboratory, Berkeley, California 94720, USA. [4]Department of Chemistry, Gakushuin University, Tokyo, Japan. [5]Earth and Planetary Sciences, University of California Santa Cruz, Santa Cruz, California 95064, USA.

Abstract

Garnet is an important mineral phase in the upper mantle as it is both a key component in bulk mantle rocks, and a primary phase at high-pressure within subducted basalt. Here, we focus on the strength of garnet and the texture that develops within garnet during accommodation of differential deformational strain. We use X-ray diffraction in a radial geometry to analyze texture development in situ in three garnet compositions under pressure at 300 K: a natural garnet ($Prp_{67}Alm_{33}$) to 30 GPa, and two synthetic majorite-bearing compositions ($Prp_{59}Maj_{41}$ and $Prp_{42}Maj_{58}$) to 44 GPa. All three garnets develop a modest (100) texture at elevated pressure under axial compression. Elasto-viscoplastic self-consistent (EVPSC) modeling suggests that two slip systems are active in the three garnet compositions at all pressures studied: {110}<1-11> and {001}<110>. We determine a flow strength of ~5 GPa at pressures between 10 to 15 GPa for all three garnets; these values are higher than previously measured yield strengths measured on natural and majoritic garnets. Strengths calculated using the experimental lattice

strain differ from the strength generated from those calculated using EVPSC. $Prp_{67}Alm_{33,}$ $Prp_{59}Maj_{41}$ and $Prp_{42}Maj_{58}$ are of comparable strength to each other at room temperature, which indicates that majorite substitution does not greatly affect the strength of garnets. Additionally, all three garnets are of similar strength as lower mantle phases such as bridgmanite and ferropericlase, suggesting that garnet may not be notably stronger than the surrounding lower mantle/deep upper mantle phases at the base of the upper mantle.

Keywords: high-pressure experiment, garnet, texture, strength, radial X-ray diffraction

Introduction

Our understanding of mantle heterogeneity and circulation is derived largely from observations of discontinuities and anisotropy in seismic wave velocities at depth. The upper mantle's seismic heterogeneity has been explained by a combination of preferred orientation of upper mantle minerals, chemically distinct previously subducted material, phase changes in minerals, and partial melting. Small scale heterogeneities have been observed via seismology (e.g., Hedlin et al. 1997), and some of those heterogeneities have been explained as subducted basaltic lithosphere via geochemical and geophysical observations (Davies 1984), and minor seismic reflections (Williams and Revenaugh 2005). By the same token, shape-preferred orientation of (likely basaltic) mantle inclusions have been invoked as one of the possible origins for mantle anisotropy. It has long been appreciated that material of basaltic chemistry is likely a common constituent of the mantle (e.g., Ringwood, 1962); it has been estimated that the upper mantle could contain subducted or delaminated basalt ranging from 5% to 40% (e.g., Allègre & Turcotte, 1986; Cammarano et al., 2009; Hirschmann & Stolper, 1996; Lundstrom et al., 2000; Schmerr et al., 2013; Williams & Revenaugh, 2005; Xu et al., 2008). The significant seismic anisotropy within the Earth's upper mantle is likely due to the shearing and stretching of

heterogeneous assemblages within the mantle, including subducted basaltic crust and depleted mantle dunite (McNamara et al. 2001). On the microscopic scale, this deformation of mantle rocks can give rise to crystallographic preferred orientation (texture). Direct observations of subducted slab anisotropy are limited due to the lack of ray paths through subducted slabs, and because the mantle wedge and sub-slab anisotropy obscure slab anisotropy due to upper mantle anisotropy. Nevertheless, there have been a few observations of anisotropy within slabs (e.g., Tian and Zhao 2012).

Hence, garnet-dominated lithologies are relevant to the mantle due to their presence in mafic and high-pressure metamorphic assemblages, such as subducted oceanic crust. Our understanding of the strength of garnets under pressure is derived largely from naturally deformed eclogites where they are resistant to plastic deformation, especially in the presence of weaker minerals like omphacite and quartz that accommodate strain (e.g., Bascou et al. 2001). In low pressure metamorphic facies, garnet is thought to deform via grain boundary sliding rather than intracrystalline deformation (e.g., Zhang & Green 2007). However, in garnet-dominated facies, like at the top of subducted slabs within the transition zone, ~90% of the volume of the crustal material is expected to be majoritic garnet; hence, understanding the deformation of the monomineralic, and especially majorite-bearing, garnet is highly relevant. Garnet has been shown to be strong compared to other mantle materials, indicating that the garnet rich zones (i.e. subducted oceanic crust) may be stronger than the surrounding mantle (Karato et al. 1995).

Garnet has a cubic structure with space group *Ia*3*d*. The garnet structure readily incorporates other chemical elements into its crystal structure; this creates extensive solid solutions and changes the stability field of, for example, majoritic garnets (with the introduction of Si). Work on the deformation of pyropic garnets has been conducted using electron

backscatter diffraction on naturally deformed eclogite assemblages. Polycrystal plasticity modeling suggests that the {110 }<1-11> slip system accommodates over 86% of strain resulting in the <100> direction aligning with the compression direction (Mainprice et al. 2004). The dominant Burgers vector for naturally deformed silicate garnets in a range of temperature regimes is ½<1-11>, which most commonly operates on the {110} plane (Voegelé et al. 1998a). This supports the results of an experimental deformation study on almandine-rich garnet where the dominant slip systems are ½<111> on {1-10}, {11-2} or {12-3}, or <100> on {010} or {011} (Voegelé et al. 1998b). Other deformation experiments on majorite-pyrope garnets with ex situ transmission electron microscopy analysis indicate Burgers vectors of <100> and ½<111> at high pressures and temperatures (Couvy et al. 2011).

A study on the strength of garnets has been conducted using high-pressure in situ X-ray diffraction in radial geometry on a natural grossular-rich garnet (Kavner 2007); however, while the strength of this garnet was characterized, the resulting textures and deformation mechanism were not investigated. Similarly, the strength of a majoritic garnet was studied within an axial configuration, but also without investigation of slip system activities (Kavner et al. 2000). Hunt et al. (2010) reported that majorite is slightly weaker than pyrope at lithospheric and upper mantle pressures and temperatures. In a comparison of olivine and pyrope, pyrope was observed to be stronger at upper mantle pressures and temperatures (Li et al. 2006). Recently, Girard et al. (2020) reported high temperature and pressure axial deformation on pyrope for use as a stress sensor material in high pressure and temperature experiments. Hence, we study the high-pressure strength and deformation of natural pyrope and synthetic pyrope-majorite garnets and report their active slip systems up to lower mantle pressures using radial diffraction in the diamond anvil cell. Our room temperature measurements provide constraints on the low-temperature strength

and slip systems of garnet, and therefore provide a low temperature bound on the rheologic behavior of garnets, while also providing insights into the compositional dependence of deformation mechanisms and strength.

Methods

Experiments were conducted on three garnets: pyrope (from the UCSC mineral collection, no. 3248, var. rhodolite from Franklin, Macon Co., North Carolina. Recently, samples from this locality have been measured to have a composition of approximately Prp60Alm37: $Prp_{58.2}Alm_{37.1}And_{1.9}Sps_{1.5}Grs_{1.3}$ (Deer et al. 1997) and $Prp_{60}Alm_{37.6}Grs_{2.9}Sps_{1.8}Uva_{0.1}$ (Hofmeister et al. 1996). Based on previous studies that quantified the water content in pyrope-almandine solid solutions from similar metamorphic environments, we estimate an upper bound of the $Prp_{67}Alm_{33}$ sample to be 0.04 wt % (Aines and Rossman 1984); this is compatible with the total derived from a wet chemical analysis of a rhodolite from this site (Deer et al. 1997). Two synthetic samples were also used: $Prp_{59}Maj_{41}$ ($Mg_3(Al_{0.59}(MgSi)_{0.41})_2(SiO_3)_4$) and $Prp_{42}Maj_{58}$ ($Mg_3(Al_{0.42}(MgSi)_{0.58})_2(SiO_3)_4$). The majorite-bearing samples were synthesized under anhydrous conditions at high pressures, and these aliquots have previously been described and characterized (Akaogi et al. 1987; McMillan et al. 1989). Infrared characterization conducted in conjunction with a prior study (McMillan et al. 1989) detected no dissolved hydroxyl within these samples, and put a bound on their water content of less than ~0.005 wt%. Gold (1-5 wt%) was used as the pressure standard (Anderson et al. 1989). $Prp_{67}Alm_{33}$ was ground for 1.5 hours with acetone in an agate mortar and pestle, followed by an additional 30 minutes with the gold to ensure even dispersal. $Prp_{59}Maj_{41}$ and $Prp_{59}Maj_{41}$ were loaded with a flake of gold present in the sample chamber. The grain size was not directly measured prior to compression; the grain size can be estimated by the crystallite size (which is refined in MAUD: Lutterotti et al. 1997) and was

between 150 and 200 Å. A BX90 style diamond anvil cell was used for diffraction with a radial geometry at 300 K. Diamonds with culets of 300 μm were used. The gasket was comprised of kapton with a boron-epoxy insert (50-80 μm thick and ~350 μm in diameter; Merkel & Yagi, 2005); the sample diameter was 60-80 μm. Sample material was inserted into the sample chamber with a stainless steel needle. In order to achieve high deviatoric stresses, no pressure medium was included in the sample chamber. Due to the fragility of the boron-epoxy gaskets on decompression, samples were not recoverable following the experiments.

Diffraction images were collected at the Advanced Light Source, beamline 12.2.2 (Kunz et al. 2005) using a MAR3450 image plate with X-rays monochromated to 25 keV (wavelength 0.4978 Å) and a sample to detector distance of ~330 mm. Wavelength, sample to detector distance, instrument broadening, peak shape, crystallite size, microstructure and texture were calibrated using the NIST standard CeO_2, and initial fits to the instrument calibrations were completed using DIOPTAS (Prescher and Prakapenka 2015), with refinements completed with the MAUD software (Lutterotti et al. 1997).

Diffraction images were processed using Fit2D (Hammersley 2016) coupled with fit2D2maud: images were unrolled by integrating over 5° azimuthal arcs, for a total of 72 spectra per diffraction image. Rietveld analysis implemented in the MAUD software (Lutterotti et al. 1997) was used to extract texture generally following the procedure for DAC data outlined in Wenk et al. (2014). Textures were calculated using the E-WIMV algorithm within MAUD, with 10° resolution for the orientation distribution function, with fiber symmetry imposed. Pole figures and inverse pole figures were smoothed and produced using BEARTEX (Wenk et al. 1998).

Lattice strain and texture development are modeled together using the elasto-viscoplastic self-consistent method (EVPSC) (Wang et al. 2010). EVPSC is an effective medium method, which treats single grains in an aggregate as inclusions in a homogeneous but anisotropic medium. The properties of the medium are determined by the average of all the inclusions. At each deformation step, the inclusions interact with the medium and the medium is updated when the average strain and stress of all inclusions equal the macroscopic stress and strain. The plastic behavior of the inclusion at the local level is described by a non-linear rate-sensitive constitutive law of various slip systems:

$$\dot{\varepsilon}_{ij} = \dot{\gamma}_0 \sum_s m_{ij}^s \left\{ \frac{|m_{kl}^s \sigma_{kl}|}{\tau^s} \right\}^n sgn(m_{kl}^s \sigma_{kl}) \quad (1)$$

Where $\dot{\varepsilon}_{ij}$ is the strain rate tensor, $\dot{\gamma}_0$ is the reference shear strain rate, τ^s is the critical resolved shear stress (CRSS) value of a slip system *s* at the reference strain rate, which controls the slip system activation. m_{kl}^s is the symmetric Schmid factor for the slip system *s*, *n* is an empirical stress exponent, and σ_{kl} is the local stress tensor. When the stress resolved onto a given slip system is close to the threshold value τ^s, deformation will occur on the slip system.

Since pressure and strain increase simultaneously in DAC experiments, it is not possible to separate the pressure and strain hardening effects on CRSS. They are both included in the pressure dependence of the CRSS. In this study, $\tau^s = \tau_0^s + d\tau/dP \cdot P + d^2\tau/dP^2 \cdot P^2$, where τ_0^s is the initial CRSS and $d\tau/dP$ and $d^2\tau/dP^2$ are the first and second order pressure dependences of CRSS. In order to simulate high pressure experimental data, a pressure dependence of the elastic moduli was used. The details for using EVPSC to simulate high pressure data can be found in Lin et al. (2017).

Results and Discussion

Differential Stress and Elasticity

X-ray diffraction data were collected on $Prp_{67}Alm_{33}$ up to 31 GPa, and on $Prp_{59}Maj_{41}$ and $Prp_{42}Maj_{58}$ up to 44 GPa. Representative experimental and calculated diffraction images are shown in Fig. S1 at 31 or 32 GPa, depending on the sample. Overall, the peaks broaden as pressure is increased; this is due to microstrain (defect structure and strain heterogeneity) within the lattice and likely crystallite size reduction. Using the four diffraction lines (400), (420), (640) and (321), which are strong and do not overlap (1) with other diffraction lines for garnet or (2) with the gold pressure standard, we are able to measure accurate values of lattice strain ($Q(hkl)$); see Text S1 and Fig. S1. The Q-values for these four lines increase at similar rates up to the highest pressures probed (Fig. 1).

Texture and Plasticity

Materials that deform brittlely at room pressure, deform ductilely at elevated pressures; a detailed discussion of this methodology can be found in Wenk et al. (2006). With increasing pressure, modest texturing (plastic deformation) is observed as demonstrated by the development of intensity variations along the Debye rings. As pressure is increased, a (100) maximum develops in the compression direction for all three compositions of garnet. On compression to 30 GPa, the pole density increases to a maximum of ~1.5 times a random distribution (m.r.d: multiples of random distribution), with a minimum of ~0.80 m.r.d. in (111) (Fig. 2) in $Prp_{67}Alm_{33}$. $Prp_{59}Maj_{41}$ and $Prp_{42}Maj_{58}$ also have a maximum of m.r.d. at (100) at 32 GPa ($Prp_{59}Maj_{41}$ and $Prp_{42}Maj_{58}$ respectively). The (100) texture remains up to the highest pressures probed for both $Prp_{59}Maj_{41}$ and $Prp_{42}Maj_{58}$ (Fig. 2). Interestingly, we do not see a difference in

texture with crystal chemistry; Voegelé et al. (1998a) also reported that even across a wide range of chemistry, similar deformation mechanisms were observed in silicate garnets.

The (100) normal aligning at high pressures to the compression direction has been observed in other garnets by Mainprice et al. (2004); however, they also found that there was a maximum of (110) poles in the compression direction. These differences indicate that the slip systems described by Mainprice et al. (2004) may not be sufficient to fully model the texture we observe. The pole figure densities (m.r.d.) are low compared to other mantle materials at similar pressures (e.g., MgO and bridgmanite; Merkel, 2002). This has been attributed to the large number (66) of possible slip systems within the garnet structure and/or a change in deformation mechanism to diffusion creep (Mainprice et al. 2004). In our experiments at room temperature, the low m.r.d. values are most likely due to the high number of symmetric variants for slip systems and relatively low strain (~20%). The previous *in situ* study of strength of grossular garnet alluded to possible plastic deformation, but did not characterize textures of deformation mechanisms (Kavner 2007).

EVPSC Modeling and Comparison to Experimental Results

We modeled the evolution of texture and lattice strain as a function of slip system activities using the EVPSC code (Wang et al. 2010). This code is advantageous because it can account for both the elastic and the viscoplastic behavior of the material by modeling lattice strain coupled with grain rotation from dislocation glide rather than only using either elastic (e.g. Elastic Plastic Self-Consistent method, EPSC; (Turner and Tomé 1994) or viscoplastic behaviors (Viscoplastic Self-Consistent method, VPSC; Lebensohn & Tomé, 1994).

With EVPSC, we tested seven slip systems : {110}<1-11>, {112}<11-1>, {123}<11-1>, {001}<110>, {011}<100>, {010}<100>, and {110}<1-10>. We imposed a strain rate of $1 * 10^{-4}$

s^{-1} as estimated by Marquardt and Miyagi (2015) for a total of ~20% strain for the $Py_{67}Alm_{33}$ and ~22% strain for $Prp_{59}Maj_{41}$ and $Prp_{42}Maj_{58}$; these values were tuned to match the observed texture intensities. We used the shear modulus reported in Sinogeikin and Bass (2000). Based on the *Q*(*hkl*) of (400), (420), (640), and (642) and the texture development with pressure, no single slip system can explain the deformation of pyrope at high pressures (Fig. S2). Only with the activation of two of these slip systems ({110}<1-11> and {001}<110>; Fig. 3**,** Table S1) can we generate the observed textures and lattice strain development in all three garnets. The experimental *Q(hkl)* values and texture are in excellent agreement with the EVPSC modeling (Fig. 3).

Elasticity

In order to compare our results with previous results for other garnets and mantle phases, we use the Voigt approximation for the uniaxial stress component,

$$t = 6G < Q(hkl) > \quad (= \sigma_3 - \sigma_1 = \sigma_Y) \qquad (2)$$

where *t* is the uniaxial stress component, *G* is the shear modulus, *Q*(*hkl*) is the lattice strain, σ_1 and σ_3 are the minimum and maximum stress, and σ_Y is the yield stress (e.g., Singh and Balasingh 1993, 1994; Singh et al. 1998). With this, we are able to estimate the flow strength and measure the elastic limit of the three garnets. We are estimating strength using this technique because it is commonly used in radial diffraction experiments; however, we will discuss that this equation overestimates the true stress in later sections. We utilize a shear modulus of 94.7 GPa and its pressure derivative d*G*/*dP* of 1.76 from Chai et al. (1997) for $Prp_{67}Alm_{33}$ and a shear modulus of 90 GPa and its pressure derivative of 1.3 for both $Prp_{59}Maj_{41}$ and $Prp_{42}Maj_{58}$ (Sinogeikin and Bass 2002). We find that all three garnets have a flow stress of ~5.5 GPa (Fig. 4, Table S2) using this approximation.

In comparing the relative strengths of these garnets, it is apparent that changes to the X and Y cations (where the standard chemistry is $X_3Y_2(SiO_3)_4$) in these samples have relatively minor effects on the elastic limit of garnet, at least in terms of Mg vs. Fe substitution into the X site and Al vs. Mg and Si substitution into the Y site. The strengths of these garnets are also comparable to those of other mantle phases derived using comparable radial diffraction techniques (Fig. 4). In all the studies we compared, the deformation was imposed using diamond anvil cells and nominally anhydrous starting materials at room temperature. These compositionally-diverse garnets having equivalent strengths at 300 K is in accord with the relative strength measurements of Hunt et al. (2010). Bridgmanite has a comparable flow strength and can accommodate similar differential stress levels up to ~20 GPa (Merkel et al., 2003), while end-member periclase is stronger than garnet at all pressures probed (Merkel, 2002). We find that pyrope is stronger than grossular garnet, as reported by Kavner (2007). We have four possible, non-exclusive explanations for this difference in strength: (1) There could be grain size differences between this study and the study of Kavner (2007); (2) there may be an intrinsic strength difference associated with Ca substitution in the X site of the garnet crystal structure; (3) there may be a higher water content/defect concentration in the grossular samples; and/or (4) the azimuthal coverage in these previous experiments may not have allowed for full characterization of the strength of the grossular garnet. With respect to this final explanation, we note that we probe from 0-360º with 5º arcs, while Kavner (2007) utilized 8 discrete angles spanning 180º and fit *Q*-values from those angles.

The experimental strength values approximated using equation (2) and those calculated using EVPSC (Fig. 4) are in excellent agreement up to ~10 GPa, and in modest agreement up until the highest pressures probed. The divergence at high pressures is common in high pressure

deformation experiments (e.g., Burnley & Zhang, 2008). Although all four of the *Q(hkl)* analyzed in this study were systematically higher than the modeled strength, there is no specific *Q(hkl)* causing the deviation at higher pressures (Fig. S3).

A limitation of diffraction-based strength studies is that they are limited by those planes satisfying the diffraction condition. As such, we are unable to measure the lattice strain of all planes within our samples, so we are inherently limiting the input for the approximation using equation (2). By using the strength calculated with EVPSC (Fig. 4), a Reuss-Voigt assumption is not imposed on the data, and we are calculating the true stress. That a difference between calculated and experimental strength exists is demonstrated by our discrepancy between experimental and modeled strengths above ~10 GPa, which increases to ~18% at 44 GPa. Our results support the assertion from Burnley & Zhang (2008) that strengths generated only with experimental lattice strain are not good proxies for the macroscopic stress of the system (Burnley & Zhang 2008).

Comparison with Previously Observed Slip Systems in Garnets

The two slip systems that are active in $Prp_{67}Alm_{33}$, $Prp_{59}Maj_{41}$, and $Prp_{42}Maj_{58}$ at high pressures have been observed in *ex situ* analysis of deformed garnets with the two most common Burgers vectors being <110> and ½<1-11>. For example, eclogitic garnets deform such that the (100) normal aligns with the compression direction and slip occurs on the {110}<1-11> system (Mainprice et al. 2004). Over our experimental pressure range, the majority (~60-64%) of the strain in pyrope is accommodated by this slip system. This Burgers vector is also consistent with the slip observed by (Voegelé et al. 1998b) in $Prp_{20}Alm_{73}Sps_2Grs_5$ on ½<111> and by Couvy et al. (2011) in $Prp_{30}Maj_{70}$. While Voegelé et al. (1998b) reported equivalent slip in the ½<1-11> direction on the {110}, {112}, and {123} planes, Mainprice et al. (2004) reported 86% of the

slip in garnets in naturally deformed eclogites occurs via the {110}<1-11> slip system. Here, we note that it is difficult to distinguish between the three slip planes {110}, {112}, and {123} due to the similarity of their textures and development of *Q*-values. Our selection of the {110} plane is partially constrained from the observation of Mainprice et al. (2004). Notably, the {110}<1-11> system appears to be active in non-silicate garnets at ambient pressure at least up to temperatures that correspond to ~0.84 of their melting temperature (Karato et al. 1994). Therefore, it appears likely that our 300 K deformation experiments access the same primary slip system as is present at high temperatures in other garnets.

The other ~40% of the strain is accommodated via the {001}<110> system. This slip system has not been observed as a major contributor to the slip in ex situ analysis of experimentally or naturally deformed garnets at high pressure/temperature conditions. For example, in natural garnets, of 50 observed dislocations, ~10 dislocations consisted of <110> type Burgers vector with glide planes of {11-1}, {22-1} or {100} (Voegelé et al. 1998a). Mainprice et al. (2004) used VPSC to identify this slip system {001}<110> as accounting for <1% of the slip in naturally deformed garnets. In passing, we note that this slip system is not geometrically distant from the dominant {110}<1-11> system: yet, the EVPSC inversion clearly distinguishes between the two sub-parallel systems. Moreover, we do not preclude that flow may involve slip on $\{110\}\frac{1}{2}$<1-11>, or via dissociated dislocations, which can be described as slip on $\{001\}\ \frac{1}{n}$<110>. Differences between the secondary slip system of this experiment and observations in garnets probed via TEM could be partially due to the difference in temperature between the high temperatures that the garnets experienced during either the experiments or metamorphism, and our 300 K experiments. Garnets analyzed in Mainprice et al. (2004) experienced pressures over 2.1 GPa and temperatures ranging from 480 ºC to >700 ºC. If this is

the case, {110}<1-11> deformation may soften under temperature relative to the {001}<110> system. Indeed, it is well known that slip system activities can change with temperature, as for example in ferropericlase (Heidelbach et al. 2003; Immoor et al. 2018). Alternatively, the secondary slip system may result from the higher pressures probed in this study compared to the TEM studies: ferropericlase, for example, activates different slip systems below 20-30 GPa and above 60 GPa (Amodeo et al. 2012; Marquardt and Miyagi 2015).

Implications

Shear wave splitting can be generated by the combination of single crystal elastic anisotropy and texturing. Brillouin spectroscopic studies of garnets have demonstrated that they remain close to elastically isotropic to high pressures. The anisotropy factor of pyrope ($2*C_{44}/(C_{11}-C_{12}) - 1$) was observed to be -0.02 at ambient conditions, and 0.01 at 14 GPa (Sinogeikin and Bass 2000). With a linear extrapolation to 30 GPa, the anisotropy would be 0.04. P- and S- wave velocities were calculated at 30 GPa with simple shear applied (100% shear strain), and using the extrapolated elastic constants from Sinogeikin and Bass [2000] and the observed texture in $Prp_{67}Alm_{33}$ (Fig. S4). Overall, the S-wave shear splitting of a polycrystalline aggregate has a maximum of 0.28% in the (100) direction. Since the shear splitting of a rock assemblage depends on each material's contribution to the shear splitting, we expect that pyropic garnet (or, by extension, similarly deforming majoritic garnets) is a silent component in terms of the possible presence of anisotropy in slabs in the upper mantle. Overall, seismic anisotropy observed in subducted slabs is likely not due to cubic solid solutions that are similar to the $Prp_{67}Alm_{33}$, $Prp_{59}Maj_{41}$, and $Prp_{42}Maj_{58}$ garnets that we have characterized. However, andradite (Jiang et al. 2004) and end-member tetragonal majorite (e.g., Pacalo & Weidner, 1997) garnets are less isotropic (as calculated from elastic tensors), and could generate modest contributions to

seismic anisotropy in the upper mantle. Nevertheless, a garnet-dominated crust of formerly basaltic chemistry is likely an isotropic cap on top of anisotropic, $(Mg,Fe)_2SiO_4$-dominated former oceanic lithosphere. Hence, there is likely substantial vertical heterogeneity in the anisotropy of subducted slabs and, based on our study, we anticipate that raypaths that dominantly traverse the crustal component of subducted slabs will show little shear wave splitting; those raypaths with moderately different trajectories sampling the dunite-enriched depleted mantle may sample much more anisotropic media.

Our *in situ* analysis of the plastic deformation and flow strength of mantle relevant $Prp_{67}Alm_{33}$ garnet to 30 GPa and $Prp_{59}Maj_{41}$, and $Prp_{42}Maj_{58}$ to 44 GPa at 300 K demonstrates that garnet is relatively strong in comparison to other mantle phases. All three garnet compositions exhibit a flow strength of 5.5 GPa at 8 GPa at 300 K, using both equation (2) and with the EVPSC results. This differs markedly from the previously reported strength of grossular garnet (Kavner 2007), and we attribute the differences to either a strong chemical dependency of garnet strength, variations in grain size, different defect contents, or a difference in data coverage; the similar strengths are in agreement with Hunt et al. (2010). Using the elasto-visco plastic self-consistent method, we identify two active slip systems: {110}<1-11> and {001}<110>. Both slip systems are needed to simultaneously match the observed lattice strain and texture development. Slip systems obtained in this study are consistent with previous ex situ analysis of deformed garnets.

These ambient temperature experiments imply that garnet-rich crustal layers on subducted slabs likely initially behave as comparatively rigid layers compared to the olivine-dominated upper mantle (particularly if the crustal layer remains relatively cold at depth). The situation within the transition zone and at the top of the lower mantle is more ambiguous,

however: both bridgmanite and periclase have strengths that generally are comparable to those that we have measured for this sequence of garnets. Similarly, ringwoodite (Kavner & Duffy, 2001) and wadsleyite (Mosenfelder et al., 2000) each have strengths that seem to be similar to those of garnet at deep transition zone conditions, as well. Accordingly, garnet-enriched regions (many of which are likely derived from basaltic protoliths) may not generate notably rheologically strong layers at the top of the lower mantle or within the deep transition zone, unless they remain colder than the surrounding mantle.

Acknowledgments

We would like to thank Jinyuan Yan for help in preparation of the gaskets and Sam Couper for useful conversations. We would like to thank the following funding sources: US NSF (EAR-1620423, EAR-1654687, EAR PF-1855336, EAR-2017294). Additional support from the US Department of Energy, National Nuclear Security Administration, through the Capital-DOE Alliance Center (DE-NA0003858). This research used resources of the Advanced Light Source (beamline 12.2.2) at Lawrence Berkeley National Laboratory which is DOE Office of Science User facility under Contract No. DE-AC02-05CH11231. This research was partially supported by COMPRES, the Consortium for Materials Properties Research in Earth Sciences under NSF Cooperative Agreement EAR 1606856.

References

Aines, R.D., and Rossman, G.R. (1984) The hydrous component in garnets: pyralspites. American Mineralogist, 69, 1116–1126.

Akaogi, M., Navrotsky, A., Yagi, T., and Akimoto, S. (1987) Pyroxene-garnet transformation: Thermochemistry and elasticity of garnet solid solutions, and application to a pyrolite mantle. In M.H. Manghnani and Y. Syono, Eds., High Pressure Research in Mineral Physics

pp. 251–260. Washington, D.C.

Allègre, C.J., and Turcotte, D.L. (1986) Implications of a two-component marble-cake mantle. Nature, 323, 123–127.

Amodeo, J., Carrez, P., and Cordier, P. (2012) Modelling the effect of pressure on the critical shear stress of MgO single crystals. Philosophical Magazine, 92, 1523–1541.

Anderson, O.L., Isaak, D.G., and Yamamoto, S. (1989) Anharmonicity and the equation of state for gold. Journal of Applied Physics, 65, 1534–1543.

Bascou, J., Barruol, G., Vauchez, A., Mainprice, D., and Egydio-Silva, M. (2001) EBSD-measured lattice-preferred orientations and seismic properties of eclogites. Tectonophysics, 342, 61–80.

Burnley, P.C., and Zhang, D. (2008) Interpreting in situ x-ray diffraction data from high pressure deformation experiments using elastic-plastic self-consistent models: An example using quartz. Journal of Physics Condensed Matter, 20.

Cammarano, F., Romanowicz, B., Stixrude, L., Lithgow-Bertelloni, C., and Xu, W. (2009) Inferring the thermochemical structure of the upper mantle from seismic data. Geophysical Journal International, 179, 1169–1185.

Chai, M., Brown, J.M., and Slutsky, L.J. (1997) The elastic constants of a pyrope-grossular-almandine garnet to 20 GPa. Geophysical Research Letters, 24, 523.

Couvy, H., Cordier, P., and Chen, J. (2011) Dislocation microstructures in majorite garnet experimentally deformed in the multi-anvil apparatus. American Mineralogist, 96, 549–552.

Davies, G.F. (1984) Geophysical and isotopic constraints on mantle convection: An interim synthesis. Journal of Geophysical Research, 89, 6017–6040.

Deer, W.A., Howie, A., and Zussman, J. (1997) Rock-Forming Minerals. Volume 1A:

Orthosilicates, 2nd ed. The Geological Society, London.

Girard, J., Silber, R.E., Mohuiddin, A., Chen, H., and Karato, S.I. (2020) Development of a stress sensor for in-situ high- pressure deformation experiments using radial x-ray diffraction. Minerals, 10, 166.

Hammersley, A.P. (2016) FIT2D: A multi-purpose data reduction, analysis and visualization program. Journal of Applied Crystallography, 49, 646–652.

Hedlin, M.A.H., Shearer, P.M., and Earle, P.S. (1997) Seismic evidence for small-scale heterogeneity throughout the Earth's mantle. Nature, 287, 145–150.

Heidelbach, F., Stretton, I., Langenhorst, F., and Mackwell, S. (2003) Fabric evolution during high shear strain deformation of magnesiowüstite ($Mg_{0.8}Fe_{0.2}O$). Journal of Geophysical Research: Solid Earth, 108, 2154.

Hirschmann, M.M., and Stolper, E.M. (1996) A possible role for garnet pyroxenite in the origin of the "garnet signature" in MORB. Contributions to Mineralogy and Petrology, 124, 185–208.

Hofmeister, A.M., Fagan, T.J., Campbell, K.M., and Schaal, R.B. (1996) Single-crystal IR spectroscopy of pyrope-almandine garnets with minor amounts of Mn and Ca. American Mineralogist, 81, 418–428.

Hunt, S.A., Dobson, D.P., Li, L., Weidner, D.J., and Brodholt, J.P. (2010) Relative strength of the pyrope-majorite solid solution and the flow-law of majorite containing garnets. Physics of the Earth and Planetary Interiors, 179, 87–95.

Immoor, J., Marquardt, H., Miyagi, L., Lin, F., Speziale, S., Merkel, S., Buchen, J., Kurnosov, A., and Liermann, H.P. (2018) Evidence for {100}<011> slip in ferropericlase in Earth's lower mantle from high-pressure/high-temperature experiments. Earth and Planetary

410 Science Letters, 489, 251–257.
411 Jiang, F., Speziale, S., Shieh, S.R., and Duffy, T.S. (2004) Single-crystal elasticity of andradite
412 garnet to 11 GPa. Journal of Physics: Condensed Matter, 16, S1041–S1052.
413 Karato, S., Wang, Z., and Fujino, K. (1994) High-temperature creep of yttrium-aluminum garnet
414 single crystals. Journal of Materials Science, 29, 6458–6462.
415 Karato, S., Wang, Z., Liu, B., and Fujino, K. (1995) Plastic deformation of garnets: systematics
416 and implications for the rheology of the mantle transition zone. Earth and Planetary Science
417 Letters, 130, 13–30.
418 Kavner, A. (2007) Garnet yield strength at high pressures and implications for upper mantle and
419 transition zone rheology. Journal of Geophysical Research, 112, 1–9.
420 Kavner, A., and Duffy, T.S. (2001) Strength and elasticity of ringwoodite at upper mantle
421 pressures. Geophysical Research Letters, 28, 2691–2694.
422 Kavner, A., Sinogeikin, S. V, Jeanloz, R., and Bass, J.D. (2000) Equation of state and strength of
423 natural majorite. Journal of Geophysical Research: Solid Earth, 105, 5963–5971.
424 Kunz, M., MacDowell, A.A., Caldwell, W.A., Cambie, D., Celestre, R.S., Domning, E.E.,
425 Duarte, R.M., Gleason, A.E., Glossinger, J.M., Kelez, N., and others (2005) A beamline for
426 high-pressure studies at the Advanced Light Source with a superconducting bending magnet
427 as the source. Journal of Synchrotron Radiation, 12, 650–658.
428 Lebensohn, R.A., and Tomé, C.N. (1994) A self-consistent viscoplastic model: prediction of
429 rolling textures of anisotropic polycrystals. Materials Science and Engineering A, 175, 71–
430 82.
431 Li, L., Long, H., Raterron, P., and Weidner, D. (2006) Plastic flow of pyrope at mantle pressure
432 and temperature. American Mineralogist, 91, 517–525.

433 Lin, F., Hilairet, N., Raterron, P., Addad, A., Immoor, J., Marquardt, H., Tomé, C.N., Miyagi, L.,
434 and Merkel, S. (2017) Elasto-viscoplastic self consistent modeling of the ambient
435 temperature plastic behavior of periclase deformed up to 5.4 GPa. Journal of Applied
436 Physics, 122.
437 Lundstrom, C.C., Gill, J., and Williams, Q. (2000) A geochemically consistent hypothesis for
438 MORB generation. Chemical Geology, 162, 105–126.
439 Lutterotti, L., Matthies, S., Wenk, H.-R., Schultz, A.S., and Richardson, J.W. (1997) Combined
440 texture and structure analysis of deformed limestone from time-of-flight neutron diffraction
441 spectra. Journal of Applied Physics, 81, 594–600.
442 Mainprice, D., Bascou, J., Cordier, P., and Tommasi, A. (2004) Crystal preferred orientations of
443 garnets: Comparison between numerical simulation and electron back-scattered diffraction
444 (EBSD) measurements in naturally deformed eclogites. Journal of Structural Geology, 26,
445 2089–2102.
446 Marquardt, H., and Miyagi, L. (2015) Slab stagnation in the shallow lower mantle linked to an
447 increase in mantle viscosity. Nature Geoscience, 8, 311–314.
448 McMillan, P., Akaogi, M., Ohtani, E., Williams, Q., Nieman, R., and Sato, R. (1989) Cation
449 disorder in garnets along the $Mg_3Al_2Si_3O_{12}$-$Mg_4Si_4O_{12}$ join: An infrared, Raman and NMR
450 study. Physics and Chemistry of Minerals, 16, 428–435.
451 McNamara, A.K., Karato, S.-I., and van Keken, P.E. (2001) Localization of dislocation creep in
452 the lower mantle: Implications for the origin of seismic anisotropy. Earth and Planetary
453 Science Letters, 191, 85–99.
454 Merkel, S. (2002) Deformation of polycrystalline MgO at pressures of the lower mantle. Journal
455 of Geophysical Research, 107, 2271.

Merkel, S., and Yagi, T. (2005) X-ray transparent gasket for diamond anvil cell high pressure experiments. Review of Scientific Instruments, 76, 046109.

Merkel, S., Wenk, H.-R., Badro, J., Montagnac, G., Gillet, P., Mao, H.K., and Hemley, R.J. (2003) Deformation of $(Mg_{0.9},Fe_{0.1})SiO_3$ perovskite aggregates up to 32 GPa. Earth and Planetary Science Letters, 209, 351–360.

Pacalo, R.E.G., and Weidner, D.J. (1997) Elasticity of majorite, $MgSiO_3$ tetragonal garnet. Physics of the Earth and Planetary Interiors, 99, 145–154.

Prescher, C., and Prakapenka, V.B. (2015) *DIOPTAS* : a program for reduction of two-dimensional X-ray diffraction data and data exploration. High Pressure Research, 1–8.

Ringwood, A.E. (1962) A model for the upper mantle. Journal of Geophysical Research, 67, 857–867.

Schmerr, N.C., Kelly, B.M., and Thorne, M.S. (2013) Broadband array observations of the 300 km seismic discontinuity. Geophysical Research Letters, 40, 841–846.

Singh, A.K., and Balasingh, C. (1993) The lattice strains in a specimen (cubic system) compressed nonhydrostatically in an opposed anvil high pressure setup. Journal of Applied Physics, 73, 4278–4286.

Singh, A.K., and Balasingh, C. (1994) The lattice strains in a specimen (hexagonal system) compressed nonhydrostatically in an opposed anvil high pressure setup. Journal of Applied Physics, 75, 4956–4962.

Singh, A.K., Balasingh, C., Mao, H., Hemley, R.J., and Shu, J. (1998) Analysis of lattice strain measured under nonhydrostatic pressure. Journal of Applied Physics, 83, 7567–7575.

Sinogeikin, S. V., and Bass, J.D. (2000) Single-crystal elasticity of pyrope and MgO to 20 GPa by Brillouin scattering in the diamond cell. Physics of the Earth and Planetary Interiors,

120, 43–62.

Sinogeikin, S. V, and Bass, J.D. (2002) Elasticity of majorite and a majorite-pyrope solid solution to high pressure: Implications for the transition zone. Geophysical Research Letters, 29, 1017.

Tian, Y., and Zhao, D. (2012) Seismic anisotropy and heterogeneity in the Alaska subduction zone. Geophysical Journal International, 190, 629–649.

Turner, P.A., and Tomé, C.N. (1994) A study of residual stresses in Zircaloy-2 with rod texture. Acta Metallurgica et Metallica, 42, 4143–4153.

Voegelé, V., Cordier, P., Sautter, V., Sharp, T.G., Lardeaux, J.M., and Marques, F.O. (1998a) Plastic deformation of silicate garnets. II. Deformation microstructures in natural samples. Physics of the Earth and Planetary Interiors, 108, 319–338.

Voegelé, V., Ando, J.I., Cordier, P., and Liebermann, R.C. (1998b) Plastic deformation of silicate garnets I. High-pressure experiments. Physics of the Earth and Planetary Interiors, 108, 305–318.

Wang, H., Wu, P.D., Tomé, C.N., and Huang, Y. (2010) A finite strain elastic-viscoplastic self-consistent model for polycrystalline materials. Journal of the Mechanics and Physics of Solids, 58, 594–612.

Wenk, H.-R., Matthies, S., Donovan, J., and Chateigner, D. (1998) BEARTEX: A Windows-based program system for quantitative texture analysis. Journal of Applied Crystallography, 31, 262–269.

Wenk, H.-R., Lutterotti, L., Kaercher, P., Kanitpanyacharoen, W., Miyagi, L., and Vasin, R. (2014) Rietveld texture analysis from synchrotron diffraction images. II. Complex multiphase materials and diamond anvil cell experiments. Powder Diffraction, 29, 220–232.

Williams, Q., and Revenaugh, J. (2005) Ancient subduction, mantle eclogite, and the 300 km seismic discontinuity. Geology, 33, 1–4.

Xu, W., Lithgow-Bertelloni, C., Stixrude, L., and Ritsema, J. (2008) The effect of bulk composition and temperature on mantle seismic structure. Earth and Planetary Science Letters, 275, 70–79.

Zhang, J., and Green, H.W. (2007) Experimental investigation of eclogite rheology and its fabrics at high temperature and pressure. Journal of Metamorphic Geology, 25, 97–115.

Fig 1

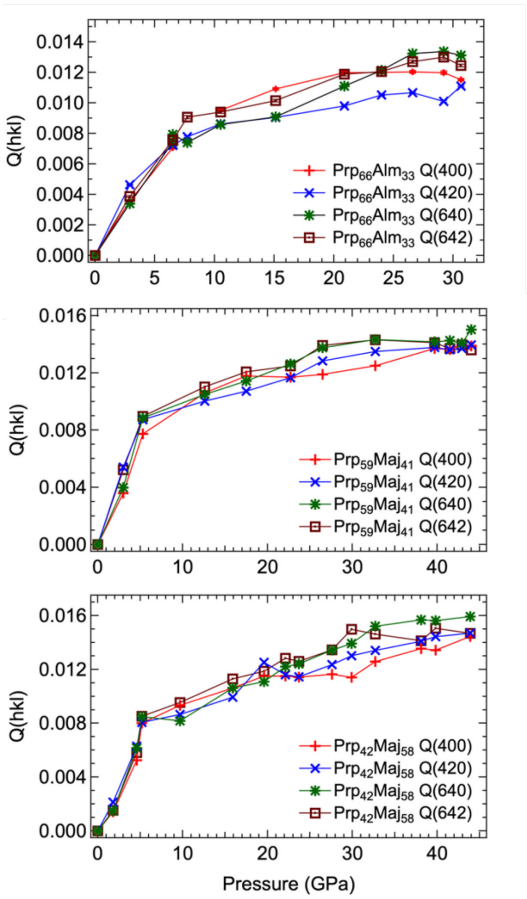

Figure 1. Experimental $Q(hkl)$ with increased pressure of the (400), (420), (640), and (642) diffraction lines for (top) $Prp_{67}Alm_{33}$, (middle) $Prp_{59}Maj_{41}$, and (bottom) $Prp_{42}Maj_{58}$.

Fig 2

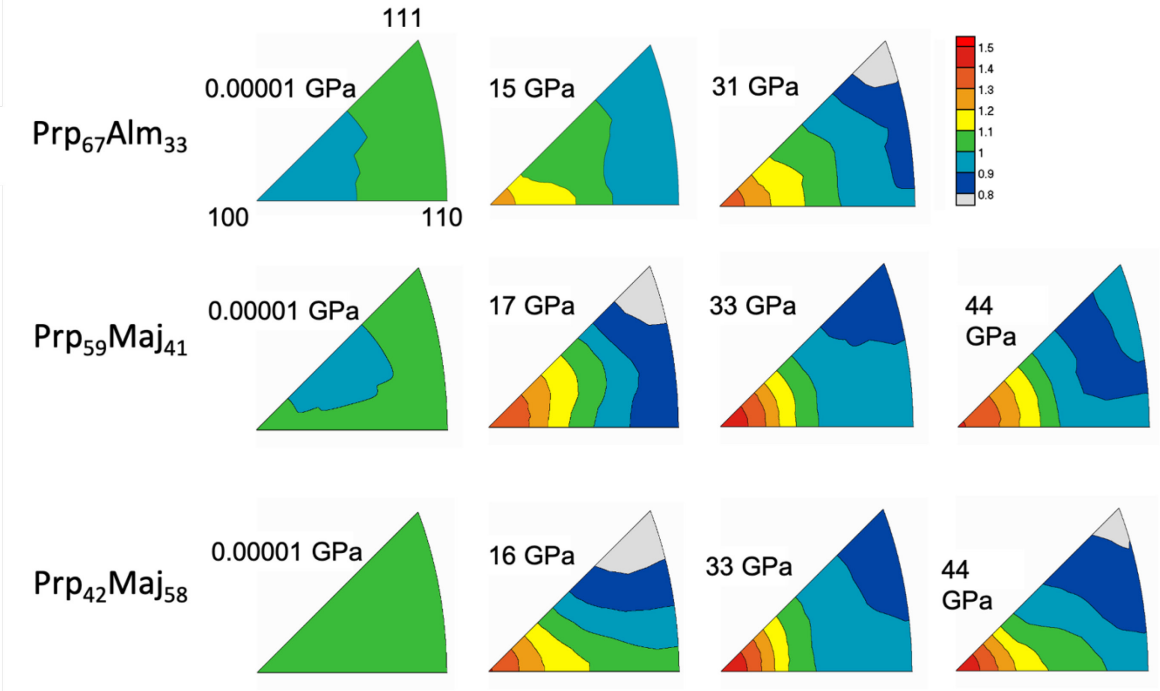

512

513 **Figure 2**. Representative inverse pole figures for the maximum compression direction of

514 $Prp_{67}Alm_{33}$, $Prp_{59}Maj_{41}$, and $Prp_{42}Maj_{58}$ at ambient pressure, ~16 GPa, ~31 GPa and 44 GPa.

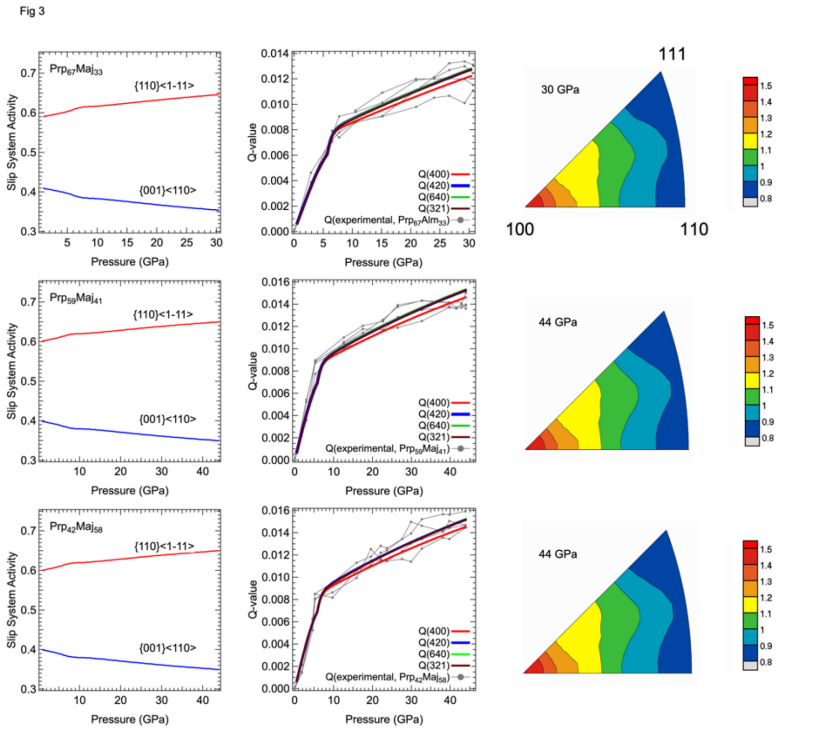

515

516 **Figure 3**. (left) Relative activity of slip systems with pressure; (middle) resulting *Q*-factors from

517 active slip systems with pressure compared to experimental *Q*-factors; and (right) inverse pole

518 figures for the maximum compression direction at the highest pressures probed for (top)

519 $Prp_{67}Alm_{33}$, (middle) $Prp_{59}Mj_{41}$, (bottom) $Prp_{42}Maj_{58}$.

520

Fig 4

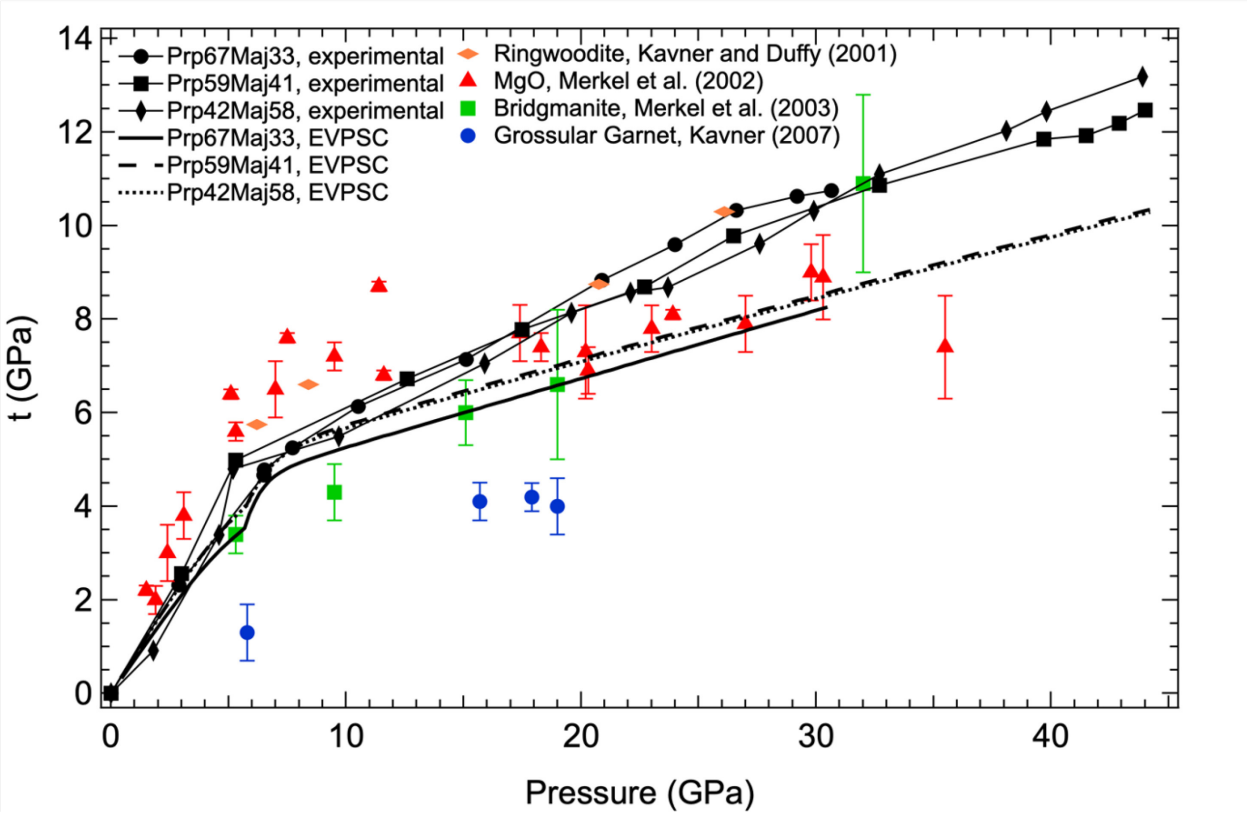

521

522 **Figure 4**. A comparison between the strength as calculated with $t = 6G < Q(hkl) >$, EVPSC

523 modeling, and other relevant mantle phases: bridgmanite (Merkel et al. 2003), MgO (Merkel

524 2002), grossular garnet (Kavner 2007), and ringwoodite (Kavner and Duffy 2001). Error bars for

525 this study are smaller than the symbols.

526